

A blind detection of a large, complex, Sunyaev–Zel’dovich structure[★]

AMI Consortium: T. W. Shimwell,^{1†} R. W. Barker,¹ P. Biddulph, D. Bly, R. C. Boysen, A. R. Brown, M. L. Brown,^{1,2} C. Clementson, M. Crofts,¹ T. L. Culverhouse,³ J. Czeres, R. J. Dace, M. L. Davies,¹ R. D’Alessandro,¹ P. Doherty,¹ K. Duggan, J. A. Ely,¹ M. Felvus, F. Feroz,¹ W. Flynn, T. M. O. Franzen,¹ J. Geisbüsch,⁴ R. Génova-Santos,⁵ K. J. B. Grainge,^{1,2} W. F. Grainger,⁶ D. Hammett,¹ M. P. Hobson,¹ C. M. Holler,⁷ N. Hurley-Walker,¹ R. Jilley, T. Kaneko, R. Kneissl,⁷ K. Lancaster,⁸ A. N. Lasenby,^{1,2} P. J. Marshall,^{9,10} F. Newton, O. Norris, I. Northrop,¹ D. M. Odell,¹ M. Olamaie,¹ Y. C. Perrott,¹ J. C. Pober,¹¹ G. G. Pooley,¹ M. W. Pospieszalski,¹² V. Quy, C. Rodríguez-González,¹ R. D. E. Saunders,^{1,2} A. M. M. Scaife,^{1,13} M. P. Schammel,¹ J. Schofield, P. F. Scott,¹ C. Shaw,¹ H. Smith,⁹ D. J. Titterton,¹ M. Velić, E. M. Waldram,¹ S. West, B. A. Wood, G. Yassin⁹ and J. T. L. Zwart¹⁴

¹*Astrophysics Group, Cavendish Laboratory, J J Thomson Avenue, Cambridge CB3 0HE*

²*Kavli Institute for Cosmology Cambridge, Madingley Road, Cambridge CB3 0HA*

³*Owens Valley Radio Observatory, California Institute of Technology, Big Pine CA 93513, USA*

⁴*National Research Council Canada, Herzberg Institute of Astrophysics, Dominion Radio Astrophysical Observatory, PO Box 248, Penticton, BC V2A 6J9, Canada*

⁵*Departamento de Astrofísica, Universidad de La Laguna, E-38205 La Laguna, Tenerife, Spain*

⁶*School of Physics and Astronomy, Cardiff University, Cardiff CF24 3AA*

⁷*Joint ALMA Office, Av El Golf, 40, Piso 18, Santiago, Chile*

⁸*H. H. Wills Physics Laboratory, University of Bristol, Tyndall Avenue, Bristol BS8 1TL*

⁹*University of Oxford, Denys Wilkinson Bldg, Keble Road, Oxford OX1 3RH*

¹⁰*Kavli Institute for Particle Astrophysics and Cosmology, Department of Physics, Stanford University, Stanford, CA 94305, USA*

¹¹*Department of Astronomy, University of California at Berkeley, Berkeley, CA 94720, USA*

¹²*NRAO Technology Center, 1180 Boxwood Estate Road, Charlottesville, VA 22903, USA*

¹³*Dublin Institute for Advanced Studies, 31 Fitzwilliam Place, Dublin 2*

¹⁴*Columbia Astrophysics Laboratory, Columbia University, 550 West 120th Street, New York, NY 10027, USA*

Accepted 2012 March 21. Received 2012 March 16; in original form 2010 December 20

ABSTRACT

We present an interesting Sunyaev–Zel’dovich (SZ) detection in the first of the Arcminute Microkelvin Imager (AMI) ‘blind’, degree-square fields to have been observed down to our target sensitivity of $100 \mu\text{Jy beam}^{-1}$. In follow-up deep pointed observations the SZ effect is detected with a maximum peak decrement greater than eight times the thermal noise. No corresponding emission is visible in the *ROSAT* all-sky X-ray survey and no cluster is evident in the Palomar all-sky optical survey. Compared with existing SZ images of distant clusters, the extent is large (≈ 10 arcmin) and complex; our analysis favours a model containing two clusters rather than a single cluster. Our Bayesian analysis is currently limited to modelling each cluster with an ellipsoidal or spherical β model, which does not do justice to this decrement. Fitting an ellipsoid to the deeper candidate we find the following. (a) Assuming that the Evrard et al. approximation to Press & Schechter correctly gives the number density of clusters as a function of mass and redshift, then, in the search area, the formal Bayesian

[★] We request that any reference to this paper cites ‘AMI Consortium: Shimwell et al. 2012’.

†Issuing author – e-mail: tws29@mrao.cam.ac.uk

probability ratio of the AMI detection of this cluster is $7.9 \times 10^4:1$; alternatively assuming Jenkins et al. as the true prior, the formal Bayesian probability ratio of detection is $2.1 \times 10^5:1$. (b) The cluster mass is $M_{T,200} = 5.5_{-1.3}^{+1.2} \times 10^{14} h_{70}^{-1} M_{\odot}$. (c) Abandoning a physical model with number density prior and instead simply modelling the SZ decrement using a phenomenological β model of temperature decrement as a function of angular distance, we find a central SZ temperature decrement of $-295_{-15}^{+36} \mu\text{K}$ – this allows for cosmic microwave background primary anisotropies, receiver noise and radio sources. We are unsure if the cluster system we observe is a merging system or two separate clusters.

Key words: galaxies: clusters: general – cosmology: observations.

1 INTRODUCTION

The Sunyaev–Zel’dovich (SZ) effect is the inverse Compton scattering of cosmic microwave background (CMB) photons from the hot plasma within clusters of galaxies (Sunyaev & Zel’dovich 1972; see e.g. Birkinshaw 1999; Carlstrom, Holder & Reese 2002 for reviews). The surface brightness of an SZ signal does not depend on the redshift z of the cluster and the integrated signal is only weakly dependent on z via the angular diameter distance. Hence an SZ-effect flux-density-limited survey can provide a complete catalogue of galaxy clusters above a limiting mass (see e.g. Bartlett & Silk 1994; Kneissl et al. 2001; Kosowsky 2003; Ruhl et al. 2004).

Detecting and imaging the SZ effect has gradually become routine since it was first securely detected by Birkinshaw, Gull & Moffet (1981) and first imaged by Jones et al. (1993). Until recently, SZ observations have been directed almost entirely towards clusters selected optically or in X-ray, for example, with AMI (AMI Consortium: Zwart et al. 2011), AMiBA (Wu et al. 2008), APEX (Halverson et al. 2009), CBI (Udomprasert et al. 2004), CBI-2 (Pearson et al. 2009), OCRA (Lancaster et al. 2007), OVRO/BIMA (Carlstrom, Joy & Grego 1996), RT(Grainge et al. 1996), SuZIE (Holzapfel et al. 1997), SZA (Muhovej et al. 2011) and the VSA (Lancaster et al. 2005). Now, however, SZ blind surveying is underway, with ACT and SPT having produced initial results (Staniszewski et al. 2009; High et al. 2010; Hincks et al. 2010; Menanteau et al. 2010; Vanderlinde et al. 2010). The Arcminute Microkelvin Imager (AMI) is conducting a blind cluster survey at 16 GHz in 12 regions, each typically 1 deg^2 , which contain no previously recorded clusters. The AMI cluster survey focuses on depth, aiming to detect weak SZ-effect signals from clusters of galaxies with a mass above $M_{T,200} = 2 \times 10^{14} M_{\odot}$, where $M_{T,200}$ corresponds to the total cluster mass within a spherical volume such that the mean interior density is 200 times the mean density of the Universe at the current epoch.

The outline of this paper is as follows. In Section 2, we give a brief description of the instrument, observations, data reduction and map-making techniques. Identifying cluster candidates is described in Section 3 – we stress that some readers will wish to jump to the start of Section 3 which is an important overview of the three analysis methods and of their assumptions. We discuss how we apply a Bayesian analysis to the AMI data in Section 4 and present the results in Section 5.

We assume a concordance Λ cold dark matter (Λ CDM) cosmology, with $\Omega_m = 0.3$, $\Omega_{\Lambda} = 0.7$ and $H_0 = 70 \text{ km s}^{-1} \text{ Mpc}^{-1}$. The dimensionless Hubble parameter h_{70} is defined as $h_{70} = H_0 / (70 \text{ km s}^{-1} \text{ Mpc}^{-1})$. All coordinates are given at equinox J2000.

2 INSTRUMENT, OBSERVATIONS, DATA REDUCTION AND MAPPING

2.1 The Arcminute Microkelvin Imager

Sited at the Mullard Radio Astronomy Observatory, Cambridge ($\approx 19 \text{ m}$ above sea level), AMI consists of a pair of aperture-synthesis interferometric arrays optimized for SZ-effect imaging centred at 16 GHz, with six frequency channels. The Large Array (LA) has a high-resolution and flux-density sensitivity and is used primarily to detect contaminating sources which can then be subtracted from the Small Array (SA) maps. AMI is described in detail in AMI Consortium: Zwart et al. (2008) and the technical aspects of the arrays are summarized in Table 1. The SA has been operating since 2005 (see e.g. AMI Consortium: Barker et al. 2006; Scaife et al. 2008; Scaife et al. 2009) and the LA since 2008 (see e.g. AMI Consortium: Hurley-Walker et al. 2009). Pointed SZ observations have been straightforward but for blind observations we have felt it essential to get the best control of systematics that we can – for example, we found hard-to-unravel problems with LA pointing and errors in the electrical lengths of the lags in both the LA and the SA Fourier transform correlators that produce small position shifts – we now have corrections for these problems that are adequate. We also have very good control over the influence of radio source contamination (see e.g. Feroz et al. 2009; AMI Consortium: Franzen et al. 2009; Waldram et al. 2010; AMI Consortium: Davies et al. 2011).

2.2 Observations

The results presented here are from observations of field AMI002 which is centred on $02^{\text{h}}59^{\text{m}}30^{\text{s}} +26^{\circ}16'30''$. AMI002 is the first field to have been analysed as it was the first to reach a target depth of $100 \mu\text{Jy beam}^{-1}$. SA observations of AMI002 began on 2008 July 19 and ran until 2010 March 3, by which time 1200 h of data had been gathered; LA observations began on 2008 August 8 and ran until 2010 January 10, collecting 630 h of data. Using both the SA and the LA the field was typically observed for 8 h in a day; this often comprised two individual observations each of 4 h, split up with an observation of a flux-density calibrator. Observations were started at different positions in the field to improve the uv coverage.

A rastering technique was used for both the LA and the SA survey observations, where the pointing centres lie on a 2D hexagonally gridded lattice. The LA observations form a part of the 10C survey data, which are described in detail in AMI Consortium: Franzen et al. (2011). Additional dedicated pointings towards the cluster

Table 1. AMI technical summary. Note that the brightness sensitivity is highly dependent on the weighting of the visibilities – in this table we assume natural weighting.

	SA	LA
Antenna diameter	3.7 m	12.8 m
Number of antennas	10	8
Number of baselines	45	28
Baseline length	5–20 m	18–110 m
16-GHz power primary beam FWHM	19.6 arcmin	5.6 arcmin
Synthesized beam FWHM	≈3 arcmin	≈30 arcsec
Array flux-density sensitivity	30 mJy s ^{-1/2}	3 mJy s ^{-1/2}
Array brightness sensitivity	4.6 mK s ^{-1/2}	16 mK s ^{-1/2}
Observing frequency	13.5–18.0 GHz	
Bandwidth	3.7 GHz	
Number of channels	6	
Channel bandwidth	0.75 GHz	
Polarization measured	<i>I</i> + <i>Q</i>	

candidates are included to ensure that maximum sensitivity was obtained in the LA maps. For the 10C survey observations, the pointing centres are separated by 4 arcmin, which allows us to obtain close-to-uniform sensitivity over the field while minimizing the observing time lost to slewing. In order to detect all important sources within the SA field, the LA field is slightly larger and the thermal noise is typically a factor of 2 lower than the SA thermal noise. To account for the SA map noise ($\sigma_{SA, survey}$) increasing towards the edge of the field, the LA map consists of two distinct regions, the inner and the outer. The inner area of the LA field was observed to a noise level of $\approx 50 \mu\text{Jy}$, whereas the noise in the outer area was approximately twice as high. The outer region of the LA map is also used to detect bright sources lying just outside the SA field. The resulting LA noise map is shown in Fig. 1. For the SA survey observations the pointing centres are separated by 13 arcmin giving a close-to-uniform noise level of $\approx 100 \mu\text{Jy}$ over the map.

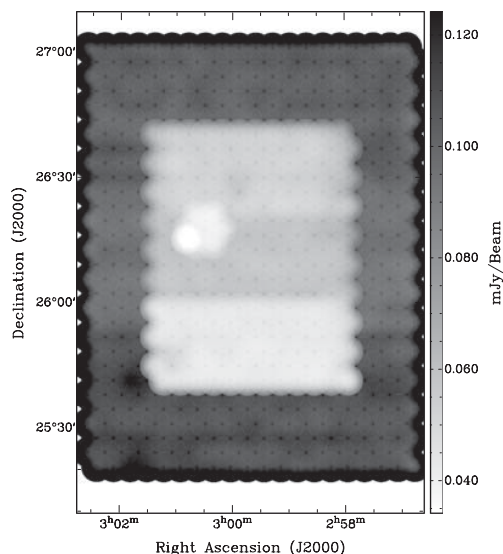


Figure 1. Noise map for the LA survey field. The inner region noise is $\approx 50 \mu\text{Jy}$, while the noise on the outer region is $\approx 100 \mu\text{Jy}$. The hexagonal region around $03^{\text{h}}00^{\text{m}}10^{\text{s}} + 26^{\circ}15'00''$ is next to the cluster and was observed to $\approx 30 \mu\text{Jy}$. The inner region of the noise map consists of three subregions; these have slightly different sensitivities due to varying weather conditions and slight differences in observing time.

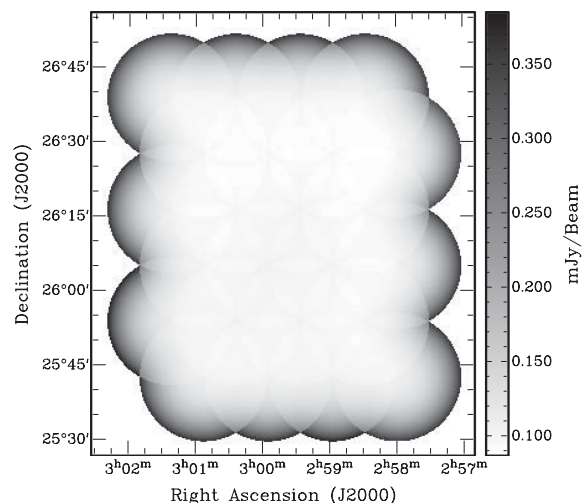


Figure 2. Noise map for the SA AMI002 field. The noise at the edge of the map increases due to the primary beam of the SA. In the central region the map noise is $\approx 100 \mu\text{Jy}$. This noise map does not include the follow-up SA observations towards $03^{\text{h}}00^{\text{m}}08^{\text{s}}66 + 26^{\circ}15'16''.1$ as those data were analysed separately. The noise level of the follow-up SA observations is $65 \mu\text{Jy}$.

Table 2. Assumed flux densities for the SA flux-density calibrators.

Channel	$\bar{\nu}$ (GHz)	S_{I+Q} (Jy)	
		3C48	3C286
1	14.2	1.850	3.663
2	15.0	1.749	3.535
3	15.7	1.658	3.414
4	16.4	1.575	3.308
5	17.1	1.500	3.206
6	17.9	1.431	3.111

The SA noise map is shown in Fig. 2. Follow-up SA observations towards the cluster consisted of 50 h of data centred at $03^{\text{h}}00^{\text{m}}08^{\text{s}}66 + 26^{\circ}15'16''.1$ resulting in a noise level of $65 \mu\text{Jy}$.

The phase calibrator was observed for 2 min every hour using the SA and for 2 min every 10 minutes using the LA. The phase calibrator used for both the LA and the SA observations was J0237+2848. The amplitude calibration for the SA uses 3C286 and 3C48 which are observed daily; the assumed flux densities are shown in Table 2 (AMI Consortium: Franzen et al. 2011). The LA was flux-density-calibrated from the SA measurements of J0237+2848; we have adopted this approach to minimize interarray calibration errors. Although the flux density of J0237+2848 is known to vary at AMI frequencies, with a mean variability index of 3.1 over 269 d (AMI Consortium: Franzen et al. 2009), we ensured that SA measurements of this source were always within 30 days of the LA observations. This calibration scheme is described in detail in AMI Consortium: Franzen et al. (2011) and provides flux-density calibration errors of less than 5 per cent.

2.3 Data reduction

There are 65 LA observations and 337 SA observations of AMI002, each being passed through `REDUCE`, the in-house software developed for the VSA and AMI data reduction. `REDUCE` was used to flag telescope pointing errors, shadowing effects and hardware errors.

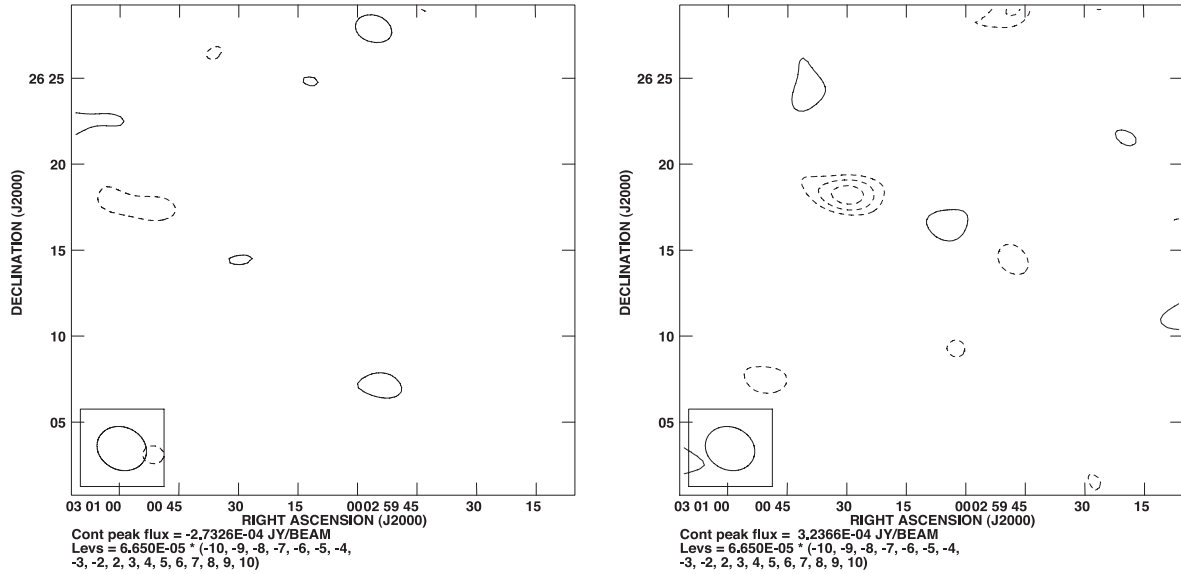


Figure 3. The jackknifed SA pointed observations of the cluster candidate (an image of the data is shown on the left of Fig. 6). On the left, data are split into plus and minus baselines, on the right, data are split according to median date. The contour levels are linear from $2\sigma_{SA,survey}$ to $10\sigma_{SA,survey}$ ($\sigma_{SA,pointed} = 65 \mu\text{Jy}$); positive contours are solid lines and negative contours are dashed lines. The ellipse at the bottom left of the maps shows the SA synthesized beam.

The data are also flagged for interference before being Fourier transformed into the frequency domain, where they are corrected for system-temperature variations, phase-calibrated and amplitude-calibrated. In the frequency domain the data are again searched for interference and baselines with inconsistent flux-density values are flagged. The data are reweighted so that baselines and channels with the lowest noise have the highest weight. The data are then stored as UVFITS files, with each raster pointing being treated as an independent source within the FITS definition. This reduction scheme follows that of AMI Consortium: Davies et al. (2009). Individual UVFITS files for the LA and the SA are combined into a single multisource UVFITS file for each array, which are taken into AIPS¹ for imaging.

The SA data were checked for systematics using two jackknife tests. In test (a), calibrated visibilities from ‘plus’ correlator boards are subtracted from those obtained from ‘minus’ correlator boards – the signal is the same for both correlations but the latter inserts an additional 180° phase shift into the signal from one antenna (see Holler et al. 2007 for a full description of the AMI correlator). For test (b), data obtained before the weighted median date of the visibilities are subtracted from data obtained afterwards. Either test will remove signals present in both halves of the data but noise or systematics that vary with time will remain. For the follow-up pointed SA observations presented in this paper test (a) revealed no systematics and test (b) showed a negative feature with a flux density of $0.35 \text{ mJy beam}^{-1}$ associated with the $2.26 \text{ mJy beam}^{-1}$ source at $03:00:29.46 +26:18:39.9$. Investigation demonstrated that this residual was a consequence of the flux density of the source being dependent upon the elongation of the synthesized beam. For reasons of scheduling, it became clear that the synthesized beam from the first half of data was elongated in the north-west–south-east direction and the source was measured to have a flux density of $2.51 \text{ mJy beam}^{-1}$. In the second half of the data the synthesized beam was extended in the north-east–south-west direction and the

measured flux density was $2.03 \text{ mJy beam}^{-1}$. Maps of the jackknifed pointed SA observations are shown in Fig. 3.

2.4 LA map making and source finding

LA maps for each AMI channel and the continuum were produced for each of the pointings within the AMI002 field using the AIPS task IMAGR. The maps are CLEANED to three times the map thermal noise without any individual CLEAN boxes. The individual pointings are combined using the FLATN task, discarding data lying outside the 10 per cent point of the power primary beam. FLATN is also used to create appropriately weighted noise maps using the thermal-noise levels in the individual pointings.

Source finding is carried out using the LA continuum map with the AMI SOURCEFIND software. All pixels on the map with a flux density greater than $0.6 \times 4 \times \sigma_n$, where σ_n is the noise map value for that pixel, are identified as peaks. The flux densities and positions of the peaks are determined using a tabulated Gaussian sinc degrading function to interpolate between the pixels. Only peaks where the interpolated flux density is greater than $4 \times \sigma_n$ are identified as sources. The AIPS routine JMFIT fits a 2D Gaussian to each source to give the angular size and the integrated flux density for the source. These fitted values are compared to the point-source response function of the telescope to determine whether the source is extended on the LA map. The mapping and the source-finding techniques are described in more detail in AMI Consortium: Franzen et al. (2011).

For each source we use the SOURCEFIND algorithm to find the flux densities in the individual AMI LA channel maps at the positions of the detected sources. By assuming a power-law relationship between flux density and frequency ($S \propto \nu^{-\alpha}$) we use the channel flux densities to determine the spectral index α for each source. The spectral index is calculated using a Markov chain Monte Carlo (MCMC) method based on that of Hobson & Baldwin (2004) – the prior on the spectral index has a Gaussian distribution with a mean of 0.5 and σ of 2.0, truncated at ± 5.0 . The minimum spectral index of a source in the AMI002 field was found to be 0.0 and the maximum was 1.8. The map noise in each channel map at the

¹ <http://www.aips.nrao.edu>

position of the source was used to calculate the weighted mean of the channel frequencies and determine the effective central frequency ν_0 of the source. The effective central frequency varies between pointings due to flagging applied in `REDUCE`. Unlike in AMI Consortium: Franzen et al. (2011), the data are not reweighted to the same frequency because this leads to a small loss of sensitivity.

In total we detect 203 sources in the AMI002 LA map at four times the LA map noise (σ_{LA}), 11 of which are extended. The most extended source has an area of 1.9 LA synthesized beams. As the SA synthesized beam is significantly larger we do not expect any extended sources in the SA map. For each source we catalogue the right ascension x_s , declination y_s , flux density at the central frequency S_0 , spectral index and the central frequency. If a source is extended we use the centroid of the fitted Gaussian as the position and the integrated flux density instead of the peak flux density.

3 IDENTIFYING AND MODELLING CLUSTER CANDIDATES

Our analysis necessarily depends in part on the fact that we do not know – in the absence of e.g. optical spectroscopic observations – the redshift of the blind SZ clusters. We have thus carried out our analysis in two main ways, both fully Bayesian and based on Hobson & Maisinger (2002), Marshall et al. (2003) and Feroz et al. (2009), as follows.

(1) Physical model. We assume an isothermal β profile for the gas density as a function of radius; we assume that all the cluster kinetic energy is in the internal energy of the cluster gas and that the relation between gas temperature and total cluster mass is then given by the virial theorem; and we assume that the prior probability for the comoving number density of clusters as a function of total mass and redshift is given by previous theoretical/simulation work – we here use the predictions of Evrard et al. (2002) and Jenkins et al. (2001) and note that more recent such work does not make a substantial difference for our purposes. With these assumptions we are then able to (a) estimate the significance of an SZ detection and (b) produce probability distributions of physical cluster parameters such as mass and radius. For both (a) and (b) the methodology takes into account radio sources, receiver noise and the statistical properties of the primordial CMB structure; it cannot take into account other effects that have not been dealt with in, for example, telescope design, telescope commissioning, observing and data reduction.

(2) Phenomenological model. Some or all of the assumptions in (1) may be poor or wholly wrong. Accordingly in (2), we make far fewer assumptions. We assume isothermality and that the temperature decrement as a function of angular distance is given by a β model. This model cannot give probability distributions of values of physical importance such as mass, but still does give the significance of the SZ detection in the presence of radio sources, receiver noise and primordial CMB structure; like (1) it cannot take into account other effects that have not previously been dealt with.

We give the significance of decrement detection in a third way, the decrement signal in units of receiver noise. We point out that for AMI this method of course takes no account of primordial CMB structures but does take into account radio sources, and the higher flux-density sources have had their SA flux densities estimated in a Bayesian way from SA data and priors from LA measurements – this allows for interarray calibration problems and for LA and SA observations that were not precisely simultaneous. Again, like (1) and (2), this method cannot take into account other effects that have not previously been dealt with.

3.1 Physical model

Our primary Bayesian analysis is based on a physical model for the cluster producing the SZ effect. The SA observations of the AMI002 survey field are analysed using a model characterized by the parameters $\Theta = (\Theta_c, \Psi)$, where $\Theta_c = (x_c, y_c, \phi, f, \beta, r_c, M_{\text{T},200}, z)$ are cluster parameters and $\Psi = (x_s, y_s, S_0, \alpha)$ are source parameters (Feroz et al. 2009). Here x_c and y_c give the cluster position, ϕ is the orientation angle measured from north through east, f is the ratio of the lengths of the semiminor to semimajor axes, β describes the cluster gas density ρ_g according to Cavaliere & Fusco-Femiano (1976, 1978), where the gas density decreases with radius r

$$\rho_g(r) = \frac{\rho_g(0)}{[1 + (r/r_c)^2]^{3\beta/2}}, \quad (1)$$

r_c is the core radius, $M_{\text{T},200}$ is the cluster total mass within a radius r_{200} and z is the cluster redshift. r_{200} is defined as the radius inside which the mean total density is 200 times the critical density ρ_{crit} . Feroz et al. (2009) and AMI Consortium: Rodríguez-González et al. (2011) describe the parameters and the methods used to extract these from the data in more detail. For this work we sample from $x_c, y_c, \phi, f, \beta, r_c, M_{\text{T},200}$ and z , and derive other cluster parameters such as the cluster gas mass $M_{\text{g},200}$ and the cluster temperature T . We also assume a mass–temperature relationship characteristic of a virialized cluster; this is the favoured model (M3) in AMI Consortium: Rodríguez-González et al. (2011), although we sample from $M_{\text{T},200}$ rather than $M_{\text{g},200}$, see also AMI Consortium: Olamaie et al. 2012. The total cluster mass within r_{200} is

$$M_{\text{T},200} = \frac{4\pi}{3} r_{200}^3 (200\rho_{\text{crit}}). \quad (2)$$

The gas fraction f_g is derived from the results of Komatsu et al. (2010) taking into account our value for h and that the gas-mass fraction is ≈ 0.9 of the baryonic mass fraction. The ellipticity of the clusters is calculated by applying a coordinate transformation from point (θ_1, θ_2) on the sky:

$$\begin{pmatrix} \theta'_1 \\ \theta'_2 \end{pmatrix} = \begin{pmatrix} \sqrt{f} & 0 \\ 0 & 1/\sqrt{f} \end{pmatrix} \begin{pmatrix} \cos \phi & \sin \phi \\ -\sin \phi & \cos \phi \end{pmatrix} \begin{pmatrix} \theta_1 \\ \theta_2 \end{pmatrix}. \quad (3)$$

Lines of constant θ' represent ellipses enclosing an area πab , where a is the semiminor axis and b is the semimajor axis. This transforms the circular slices perpendicular to the line of sight to an ellipse, keeping the area of the ellipse the same as the circular slice. A summary of the priors used on the model parameters is shown in Table 3.

The above approach has already been used to detect the SZ effect from AMI observations of known clusters in AMI Consortium: Zwart et al. (2011) and AMI Consortium: Rodríguez-González et al. (2011). However, for blind cluster surveys we are faced with the additional problem that we do not have a priori evidence for a cluster at a particular position (or redshift). In analysing a survey field, the marginalized posterior distribution in the (x_c, y_c) plane will typically contain a number of local peaks; some of these may correspond to the presence of a real cluster, whereas others may result from chance statistical fluctuations in the primordial CMB and/or instrument noise. Each local peak in the posterior is automatically identified by the MULTINEST sampler (Feroz & Hobson 2008; Feroz, Hobson & Bridges 2008) used in our Bayesian analysis, and may subsequently be analysed independently to obtain cluster parameter estimates.

To determine the significance of each such putative cluster detection, we perform a Bayesian model selection, which makes use

Table 3. Priors used for the Bayesian analysis assuming a physical cluster model.

Parameter	Prior
Source position (x_s)	A delta-function prior using the LA positions
Source flux density (S_0/Jy)	A Gaussian centred on the LA continuum value with a σ of 40 per cent
Source spectral index (α)	A Gaussian centred on the value calculated from the LA channel maps with the LA error as σ
Redshift (z)	Joint prior with M_T between 0.2 and 2.0 (Jenkins et al. 2001 or Evrard et al. 2002)
Core radius (r_c/h_{70}^{-1} kpc)	Uniform between 10 and 1000
Beta (β)	Uniform between 0.3 and 2.5
Mass ($M_{T,200}/h_{70}^{-1} M_\odot$)	Joint prior with z between 2.0×10^{14} and 5×10^{15} (Jenkins et al. 2001 or Evrard et al. 2002)
Gas fraction (f_g/h_{70}^{-1})	Delta-function prior at 0.11 (Komatsu et al. 2010)
Cluster position (\mathbf{x}_c)	Uniform search triangle (Fig. 4)
Orientation angle [ϕ (deg)]	Uniform between 0 and 180
Ratio of the length of semiminor to semimajor axes (f)	Uniform between 0.5 and 1.0

of estimated cluster number counts from analytical theory (e.g. the Evrard et al. 2002 approximation to Press & Schechter 1974) and numerical modelling (e.g. Jenkins et al. 2001) together with measurements of the rms mass fluctuation amplitude on scales of size $8 h_{100}^{-1}$ Mpc at the current epoch (see e.g. Lahav et al. 2002; Seljak et al. 2005; Vikhlinin et al. 2009). It must be borne in mind, however, that the actual values of the number density of clusters, particularly at high redshift, are uncertain and hence the degree of applicability of these as priors is unclear.

In our Bayesian model selection, we calculate the formal Bayesian probability of two hypotheses: the first, $\Pr(H_{\geq 1}|D)$, assumes that at least one cluster with $M_{T,\text{lim}} < M_{T,200} < M_{T,\text{max}}$ is associated with the local peak in the posterior distribution under consideration; the second, $\Pr(H_0|D)$, assumes that no such cluster is present. Here $M_{T,\text{lim}}$ is the limiting cluster mass that can be detected and $M_{T,\text{max}}$ is the maximum mass of a cluster. In particular, we consider the ratio R (also known as the Bayes factor, or the odds) of these two formal probabilities:

$$R \equiv \frac{\Pr(H_{\geq 1}|D)}{\Pr(H_0|D)}. \quad (4)$$

To evaluate this ratio, let us first denote by S the area in the (x_c, y_c) plane of the ‘footprint’ of the local posterior peak under consideration (we will see below that a precise value for S is not required). Also, we denote by H_n the hypothesis that there are n clusters with $M_{T,\text{lim}} < M_{T,200} < M_{T,\text{max}}$ with centres lying in the footprint S , so that

$$\Pr(H_{\geq 1}) = \sum_{n=1}^{\infty} \Pr(H_n). \quad (5)$$

Thus equation (4) can be written as

$$R = \frac{\sum_{n=1}^{\infty} \Pr(H_n|D)}{\Pr(H_0|D)} = \frac{\sum_{n=1}^{\infty} \Pr(D|H_n) \Pr(H_n)}{\Pr(D|H_0) \Pr(H_0)}, \quad (6)$$

where we have used Bayes’ theorem in the second equality. Assuming that objects are randomly distributed over the sky, then

$$\Pr(H_n) = \frac{e^{-\mu_S} \mu_S^n}{n!}, \quad (7)$$

where μ_S is the expected number of clusters with $M_{T,\text{lim}} < M_{T,200} < M_{T,\text{max}}$ in a region S . This is given by $\mu_S = S\mu$, where μ is the expected number of clusters per unit sky area:

$$\mu = \int_{z_{\text{min}}}^{z_{\text{max}}} \int_{M_{T,\text{lim}}}^{M_{T,\text{max}}} \frac{d^2 n}{dM dz}, \quad (8)$$

where $n(z, M)$ is the comoving number density of clusters as a function of redshift and mass. For the calculation of μ , we follow

the method of either Evrard et al. (2002) or Jenkins et al. (2001). If we further assume that there is very low probability of two or more clusters having their centres in the region S ($\mu_S \ll 1$) we can neglect μ_S^2 and larger powers of μ_S , so that equation (6) can be approximated simply by

$$R \approx \frac{Z_1(S)\mu_S}{Z_0}, \quad (9)$$

where the $Z_1(S) = \Pr(D|H_1)$ is the ‘local evidence’ (see Feroz et al. 2009) associated with the posterior peak under consideration in the single-cluster model, and $Z_0 = \Pr(D|H_0)$ is the ‘null’ evidence (which does not depend on S).

Our Bayesian analysis uses MULTINEST to calculate the Bayesian evidence for the different hypotheses (Feroz & Hobson 2008; Feroz et al. 2008). When searching for clusters in some survey area A , however, a uniform prior $\pi(x_c, y_c) = 1/A$ is assumed on the position of any cluster, rather than assuming a uniform prior over the footprint S . Thus, MULTINEST returns a local evidence associated with the posterior peak that is given by

$$\tilde{Z}_1(S) = \frac{S}{A} Z_1(S), \quad (10)$$

and the ‘null’ evidence $\tilde{Z}_0 = Z_0$ remains unchanged. Thus, if we denote the expected number of clusters in the survey area by $\mu_A = (A/S)\mu_S$, then (6) becomes

$$R \approx \frac{\tilde{Z}_1(S)\mu_A}{\tilde{Z}_0}. \quad (11)$$

Here $\tilde{Z}_1(S)$ and \tilde{Z}_0 are outputs of MULTINEST and μ_A is easily calculated from (8) given some assumed cluster mass function, and so R may then be calculated. In our analysis $\mu_A < 1$ and the R value that we calculate is smaller than that obtained by setting the prior ratio equal to unity. Jeffreys (1961) provides an interpretive scale for the R value, as do revised scales such as Gordon & Trota (2007). Moreover, the R value in (11) can be turned into a formal Bayesian probability p that the putative detection is indeed due to a cluster with mass $M_{T,\text{lim}} < M_{T,200} < M_{T,\text{max}}$ and centre lying in S , which is given by

$$p = \frac{R}{1+R}. \quad (12)$$

3.2 Phenomenological model

An alternative approach is to set aside the physical cluster model and instead adopt a model based on a phenomenological description of the SZ decrement itself.

Table 4. Priors used for the Bayesian analysis assuming a phenomenological cluster model.

Parameter	Prior
ΔT_0	Uniform between $\pm 3000 \mu\text{K}$
θ_c	Uniform between 20 and 500 arcsec
β	Uniform between 0.4 and 2.5

In this case, at the location of each putative cluster detection identified using the physical cluster model, we simply fit a β profile to the SZ temperature decrement using the parameters θ_c , β and ΔT_0 to characterize shape and magnitude of the decrement according to

$$\Delta T_{\text{SZ}} = \Delta T_0 \left(1 + \frac{\theta^2}{\theta_c^2} \right)^{(1-3\beta/2)}. \quad (13)$$

The assumed priors on these parameters are summarized in Table 4. In this analysis we continue to use Gaussian priors on the flux densities and on the spectral indices of significant sources, and delta-function priors for faint sources. We also assume a Gaussian prior ($\sigma = 60$ arcsec) on position centred on each decrement.

This approach allows us to produce a posterior distribution that directly describes the temperature decrement and also allows us to evaluate what proportion of the decrement is caused by the SZ effect, while also accurately accounting for point sources, receiver noise and the statistical properties of the primary CMB anisotropy.

4 THE ANALYSIS

The AMI002 SA survey map contains 24 individual pointing centres. A single Bayesian analysis of the entire field is prohibitively computationally expensive because of the large quantity of data and the high dimensionality of the parameter space. Instead three pointings are analysed at a time. Each set of three pointing centres forms a triangle and in total there are 30 different triangles in the AMI002 field, an example of which is shown in Fig. 4.

To reduce the dimensionality of the parameter space further, all sources located at positions where the primary beam has fallen below 10 per cent of its maximum, together with sources that have a flux density measured on the LA that is lower than $4\sigma_{\text{SA,survey}}$, are given delta-function priors on their positions, spectral indices

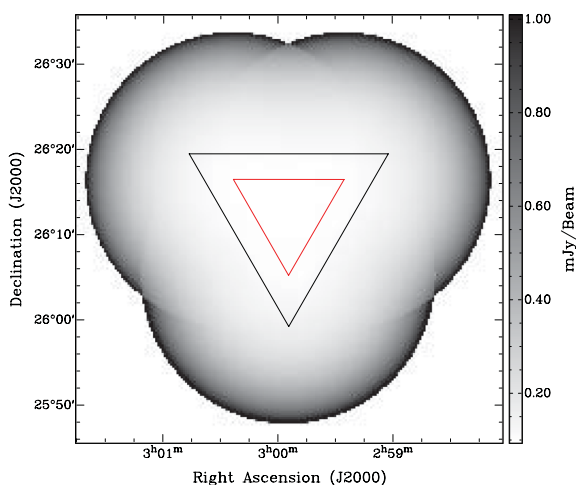


Figure 4. Noise map for a SA triangle of observations out to the 0.1 contour of the power primary beam. The inner triangle is between the pointing centres; the outer triangle is the area that is searched for clusters with our Bayesian analysis.

and flux densities. We search for clusters in a triangular area which is an enlarged version of the triangle formed between the pointing centres – the radius of the inscribed circle is 3 arcmin larger. This allows us to detect clusters out to the edge of our most sensitive areas and ensures that the search areas belonging to adjacent triangles overlap. The minimum rms noise within a search triangle in the AMI002 field is $\approx 100 \mu\text{Jy}$ and the maximum is $\approx 140 \mu\text{Jy}$. The limiting cluster total mass is set to $M_{\text{T,lim}} = 2 \times 10^{14} h_{70}^{-1} M_{\odot}$ and the maximum cluster mass to $M_{\text{T,max}} = 5 \times 10^{15} h_{70}^{-1} M_{\odot}$. The limiting mass is conservative given the radio flux-density sensitivity of our observations.

We follow up our most significant detections with pointed observations towards the candidate. The data from these observations can be analysed with our Bayesian method with lower dimensionality because there are fewer sources within 0.1 of the power primary beam with flux densities greater than $4\sigma_{\text{SA,pointed}}$. For the follow-up pointed observations the prior on the cluster position is altered to a 1000×1000 arcsec² box centred on the pointing centre and we allow our Bayesian analysis software to fit the source positions with a Gaussian prior centred on the LA position with an error of 5 arcsec.

5 RESULTS AND DISCUSSION

The most significant candidate cluster detection made using the Bayesian analysis of the AMI SA survey field AMI002 is located at J 03^h00^m16.5 +26° 13'59".5, where MULTINEST identifies a single marginalized posterior peak in the (x_c, y_c) plane centred on this location. The significance of the cluster detection is $R \approx 8.7$ when we use Model (1) and the Evrard et al. (2002) prior, and $R \approx 26$ when we apply Model (1) using the Jenkins et al. (2001) prior. The relevant area of the survey field is shown in Fig. 5 before and after source subtraction (see below). In the search triangle that contains our cluster candidate there are 59 sources within 0.1 of the power primary beam, 43 of which have a flux density below $4\sigma_{\text{SA,survey}}$; the other 16 have been modelled with our Bayesian analysis. The location of the marginalized posterior peak is indicated by the small box in the figures.

At this position in our survey field is a highly extended, non-circular negative feature with a peak flux-density decrement of ≈ 0.6 mJy ($5\sigma_{\text{SA,survey}}$). SA observations are mapped in AIPS using the same method as for the LA, but with a pixel size of 15 arcsec. We subtract sources from the UVFITS data using the in-house software MUESLI. MUESLI performs the same function as the AIPS task UVSUB; however, it is optimized for processing AMI data. The parameters of the 16 modelled sources are shown in Table 5; we find no evidence that any of them is extended relative to the LA synthesized beam. The source subtraction leaves very little residual flux density on the map, indicating that the phase stability and calibration of AMI are robust. The most significant source-subtraction residuals are towards the edge of the SA power primary beam where we expect the phase errors to be larger and the beam model to be less accurate.

The cluster candidate was followed up with a pointed observation. Within the 10 per cent point of the SA power primary beam 31 sources were observed with the LA, nine of which were detected at above $4\sigma_{\text{SA,pointed}}$ and are modelled by our Bayesian analysis. These nine sources are a subset of the 16 sources modelled on the Bayesian analysis of the survey data; they are indicated by a ‘tick’ in the last column of Table 5. We find no evidence that any of these nine sources is extended relative to the LA synthesized beam. The image produced from the pointed-observation data is shown before and

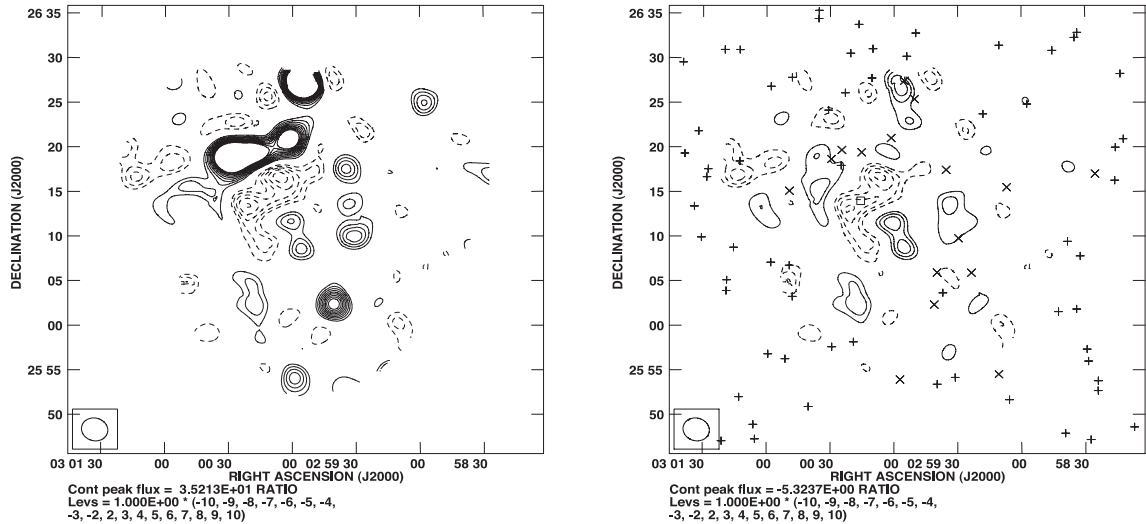


Figure 5. The SA survey-field observations of the cluster candidate. On the left is the map before source subtraction and on the right is the map after the sources in Table 5 have been subtracted. The + symbols indicate the positions of sources with flux densities less than $4\sigma_{SA,survey}$ and the × symbols represent sources which have a flux density greater than $4\sigma_{SA,survey}$. The box on the source-subtracted map shows the position of the cluster candidate. These maps are signal-to-noise ratio maps. Each pointing has a thermal-noise level of approximately 0.11 mJy. The contour levels are linear from $2\sigma_{SA,survey}$ to $10\sigma_{SA,survey}$; positive contours are solid lines and negative contours are dashed lines. The ellipse at the bottom left of the maps shows the SA synthesized beam.

Table 5. The fitted parameters for the 16 sources with LA flux densities greater than $4\sigma_{SA,survey}$ ($65 \mu\text{Jy}$). This includes the nine sources with flux densities greater than $4\sigma_{SA,pointed}$. The positions and mean frequencies are from LA observations, whereas the flux densities and spectral indices are the values obtained from our Bayesian analysis of the SA survey field.

Right ascension (J2000)	Declination (J2000)	Flux density (mJy)	Spectral index	Mean frequency (GHz)	Flux density $>4\sigma_{SA,pointed}$
03:00:24.53	+26:19:40.83	1.21 ± 0.12	$+1.38 \pm 0.38$	15.63	✓
03:00:29.46	+26:18:39.95	2.26 ± 0.12	$+0.71 \pm 0.29$	15.64	✓
02:59:06.92	+26:15:29.59	0.26 ± 0.09	$+1.46 \pm 1.10$	15.57	✓
02:59:50.35	+26:25:22.37	0.23 ± 0.11	$+0.51 \pm 1.24$	15.58	×
02:59:39.76	+26:05:56.15	0.40 ± 0.09	$+2.31 \pm 1.06$	15.52	×
03:00:15.23	+26:19:25.56	1.44 ± 0.11	$+1.59 \pm 0.40$	15.64	✓
02:59:23.57	+26:05:54.53	0.40 ± 0.10	$+0.81 \pm 1.24$	15.54	×
02:59:55.16	+26:27:26.24	8.49 ± 0.22	$+0.33 \pm 0.07$	15.59	✓
02:59:10.71	+25:54:31.60	3.81 ± 0.41	$+1.05 \pm 0.16$	15.57	×
02:59:35.43	+26:17:26.77	0.64 ± 0.09	-0.22 ± 0.94	15.53	✓
03:00:49.28	+26:15:05.70	0.53 ± 0.12	$+0.40 \pm 0.42$	15.67	✓
02:59:29.68	+26:09:46.99	0.50 ± 0.07	$+1.71 \pm 1.26$	15.55	×
02:59:41.05	+26:02:20.41	1.58 ± 0.12	$+1.36 \pm 0.36$	15.54	✓
02:59:57.17	+25:53:56.17	1.40 ± 0.23	$+2.20 \pm 0.34$	15.58	×
03:00:01.33	+26:21:01.55	1.96 ± 0.12	-0.45 ± 0.31	15.56	✓
02:58:25.32	+26:16:59.59	1.63 ± 0.33	$+0.95 \pm 0.27$	15.58	×

after source subtraction in Fig. 6. Again we see a highly extended, non-circular negative feature with a peak flux-density decrement of ≈ 0.6 mJy ($8\sigma_{SA,pointed}$). The SA synthesized beam and the uv coverage for the follow-up pointed observation are shown in Fig. 7. To estimate the maximum level of contamination from the residuals of the sources in Table 5 we assume that the residual is equal to the error in the source flux, we then sum the absolute value of the synthesized beam contribution from each of these residuals at the positions of candidates 1 and 2, we find contributions of 32 and $70 \mu\text{Jy}$, respectively. Hence, if in the unlikely case all sources leave a feature of magnitude equal to the error in that source flux, and that these features conspire in such a way to contribute only negative flux at the positions of candidates 1 and 2, we find that the contribution

to the total SZ signal is minimal. This calculation does not account for any errors in the shape of the synthesized beam, due to e.g. antenna positions.

Our Bayesian analysis of the pointed-observation data, which has a higher signal-to-noise ratio than the survey data, finds *two* local peaks in the marginalized posterior distribution in the (x_c, y_c) plane. These cluster candidates are as follows: candidate 1 at J 03^h00^m14^s.8 +26° 10′ 02″.6 and candidate 2 at J 03^h00^m08^s.9 +26° 16′ 29″.1. The Model (1) significance of the two cluster detections are $R_1 \approx 7.9 \times 10^4$ and $R_2 \approx 560$, respectively, when we apply the Evrard et al. (2002) model and $R_1 \approx 2.1 \times 10^5$ and $R_2 \approx 1800$, respectively, when we apply the Jenkins et al. (2001) model. These larger values for the R ratio, as compared with those obtained

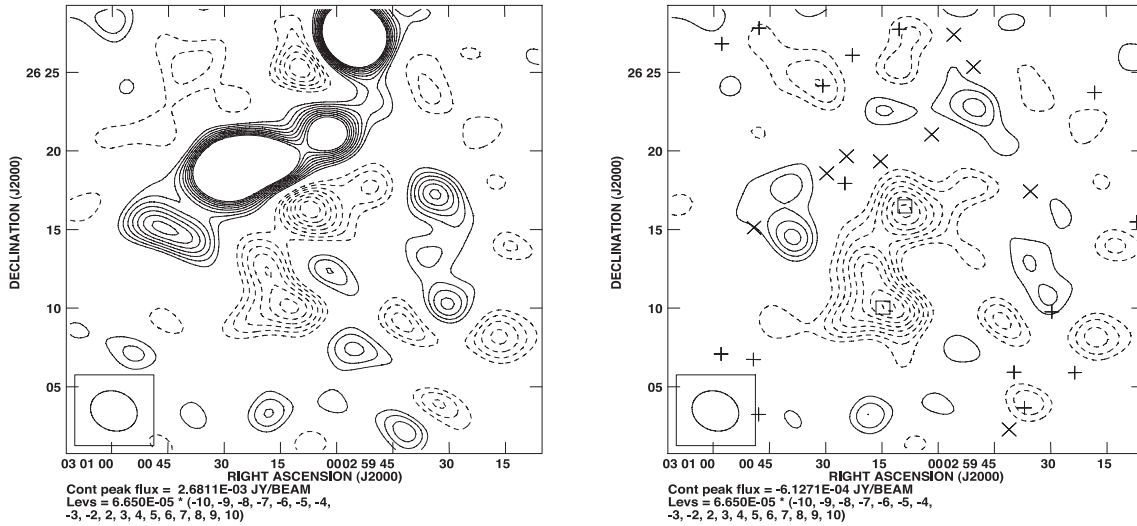


Figure 6. The AMI SA pointed observation towards the cluster. On the left is the map before source subtraction and on the right is the map after the relevant sources in Table 5 have been subtracted. The + symbols indicate the positions of sources with flux densities less than $4\sigma_{\text{SA,pointed}}$, the \times symbols represent sources which have a flux density greater than $4\sigma_{\text{SA,pointed}}$ on the SA map. For this run, the sampler has been allowed to fit the positions of the \times type sources with a Gaussian centred on the LA source position. The contour levels are linear from $2\sigma_{\text{SA,pointed}}$ to $10\sigma_{\text{SA,pointed}}$ ($\sigma_{\text{SA,pointed}} = 65 \mu\text{Jy}$); positive contours are solid lines and negative contours are dashed lines. The boxes indicate the positions of the cluster candidates. Candidate 1 is at $J 03^{\text{h}}00^{\text{m}}14^{\text{s}}.8 + 26^{\circ}10'02''.6$ and candidate 2 is at $J 03^{\text{h}}00^{\text{m}}08^{\text{s}}.9 + 26^{\circ}16'29''.1$. When imaging the source-subtracted map CLEAN boxes have been placed around each candidate. The ellipse at the bottom left of the maps shows the SA synthesized beam.

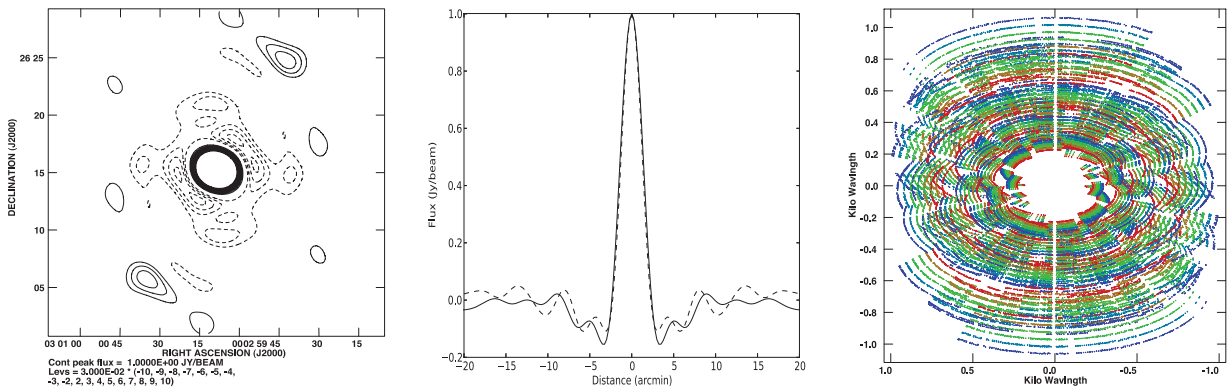


Figure 7. On the left is the synthesized beam for the AMI SA pointed observation towards the cluster (Fig. 6). The contour levels range from 6 to 30 per cent with intervals of 3 per cent; positive contours are solid lines and negative contours are dashed lines. The image in the centre shows 1D slices through the centre of the synthesized beam; dashed lines show the profile along the declination axis and solid lines show the profile along the right ascension axis. The image on the right shows the corresponding uv coverage of the observation; a different colour is used for each AMI channel.

using the survey data, result from the higher signal-to-noise ratio of the pointed observation. The evidence values, R ratios and related parameters for the survey observations and the pointed observation are summarized in Table 6. We also made a direct comparison of the Bayesian evidence for a model containing two clusters and a model containing just a single cluster and find that the Bayesian evidence is 7.6×10^5 higher for the model containing two clusters.

The 1D and 2D marginal posterior distributions for a selection of the physical parameters of each cluster are shown in Fig. 8. We are able to constrain $M_{\text{T},200}$, even though it is degenerate with z . As $M_{\text{T},200}$ is large this degeneracy causes the derived z value to be low. We are able to constrain the well-known degeneracy between β and r_c and find that values of $\beta < 1.0$ do not fit our data. We also find that the best-fitting ratios of the lengths of the semiminor to semimajor axes are 0.6 and 0.75, respectively; the orientation angles are 122° and 78° .

Table 6. Evidences, R ratios and related parameters for the detection of the cluster candidates in the triangle of survey observations and the follow-up deep pointed observation. The limiting total mass is $M_{\text{T,lim}} = 2 \times 10^{14} h_{70}^{-1} M_\odot$.

Parameter	Survey	Pointed (candidate 1)	Pointed (candidate 2)
Search area (sr)	2.00×10^{-5}	2.35×10^{-5}	2.35×10^{-5}
$\log(\tilde{Z}_{1,\text{Jenkins}})$	56 351.1	29 692.1	29 687.3
$\log(\tilde{Z}_{1,\text{Evrard}})$	56 350.9	29 692.0	29 687.1
$\log(\tilde{Z}_0)$	56 346.6	29 678.8	29 678.8
μ_s, Evrard	0.11	0.14	0.14
$\mu_s, \text{Jenkins}$	0.29	0.34	0.34
R_{Press}	8.7	7.9×10^4	560
R_{Jenkins}	26	2.1×10^5	1800

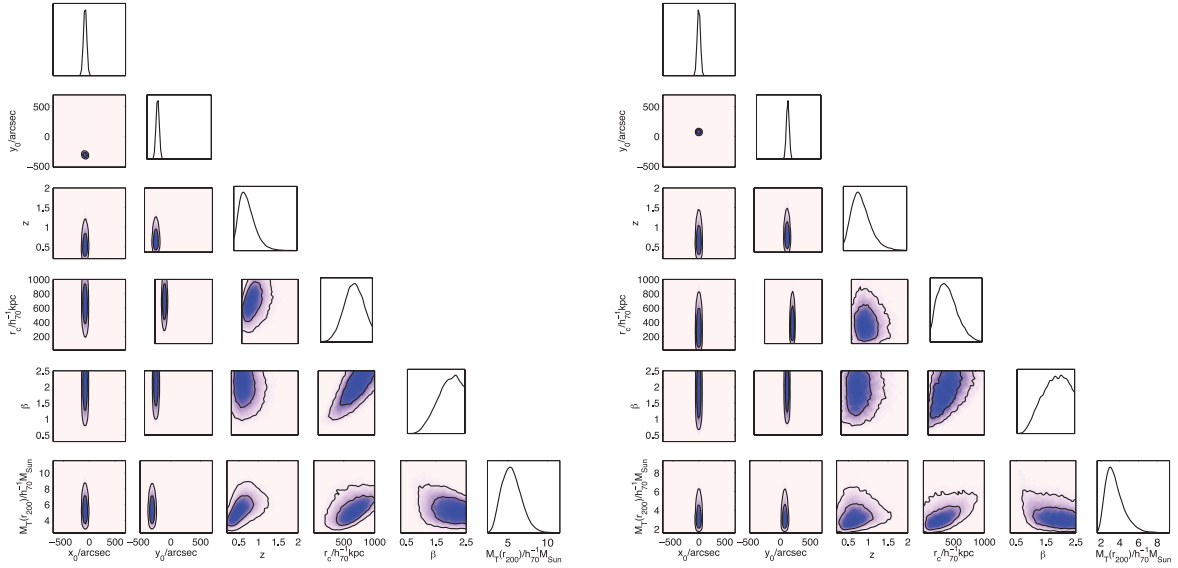


Figure 8. 1D and 2D marginal posterior distributions for a selection of the parameters in physical cluster model for candidate 1 (left) and candidate 2 (right). The $M_{T,200}$ values have been divided by 10^{14} .

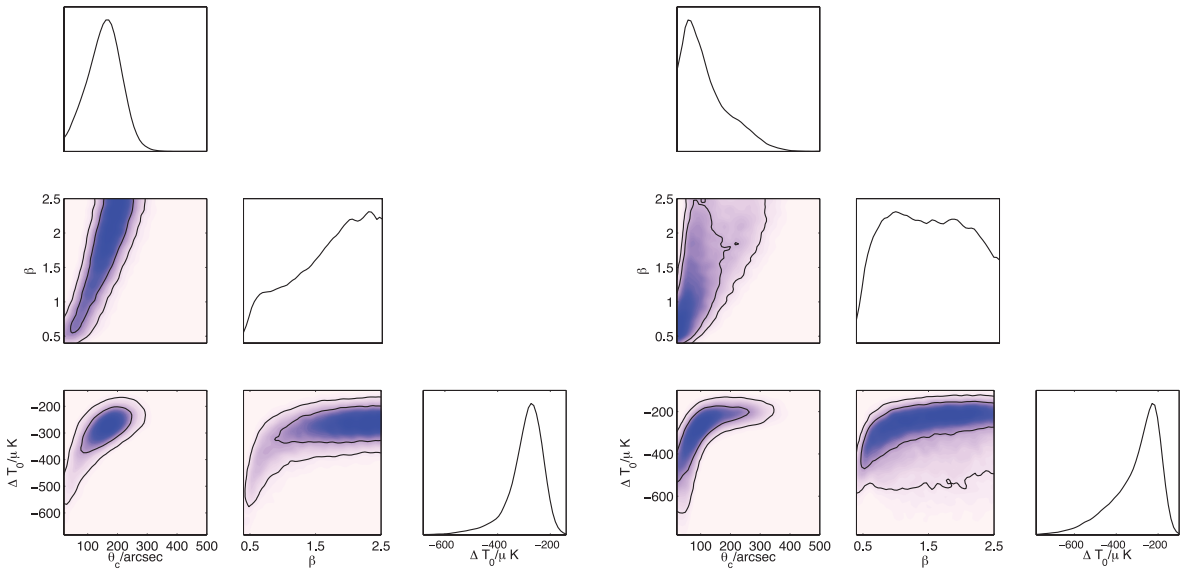


Figure 9. 1D and 2D marginal posterior distributions for the parameters in the SZ decrement model for candidate 1 (left) and candidate 2 (right).

Finally, we used Model (2) and performed a Bayesian analysis where we simply fit a β profile to the SZ temperature decrement directly. The 1D and 2D marginal posterior distributions for the parameters θ_c , β and ΔT_0 are shown in Fig. 9. From our data we are able to tightly constrain ΔT_0 at ≈ -300 μK , but we are unable to accurately derive β . The mean values and 68 per cent confidence limits for each parameter are given in Table 7 and demonstrate significance of the detections directly.

We have looked for optical identification of the cluster in the Palomar all-sky survey and X-ray identification from *ROSAT*² – no cluster identification is evident. We plan to perform X-ray and optical follow-up observations.

² We have made use of the *ROSAT* Data Archive of the Max-Planck-Institut für extraterrestrische Physik (MPE) at Garching, Germany.

Table 7. Mean values and 68 per cent confidence limits for the parameters in the SZ decrement model for candidates 1 and 2.

Parameter	Pointed (candidate 1)	Pointed (candidate 2)
θ_c (arcsec)	156^{+27}_{-25}	121^{+19}_{-100}
β	$1.60^{+0.81}_{-0.24}$	$1.46^{+1.03}_{-1.06}$
ΔT_0 (μK)	-295^{+36}_{-15}	-302^{+70}_{-27}

6 CONCLUSIONS

(i) We have presented a large, complex SZ structure in an AMI blind field. The structure may be two separate components or be a single merging system.

(ii) A Bayesian analysis using a physical model for the cluster (including assumed priors on the number density of clusters) was used to constrain cluster parameters such as β , r_c , $M_{T,200}$ and z . Using the Bayesian evidences we have calculated formal probabilities of detection taking into account point sources, receiver noise and the statistical properties of the primary CMB anisotropy. For the deeper component we find a formal probability of detection ratio of $7.9 \times 10^4:1$ when assuming the Evrard et al. (2002) cluster number count and $2.1 \times 10^5:1$ when assuming Jenkins et al. (2001) as the true prior. We derive a cluster mass of $M_{T,200} = 5.5^{+1.2}_{-1.3} \times 10^{14} h_{70}^{-1} M_{\odot}$.

(iii) A Bayesian analysis using a phenomenological model of the gas distribution was also used to quantify the significance of the detection and again taking into account point sources, receiver noise and the statistical properties of the primary CMB anisotropy. For the deeper component we find $\Delta T_0 = -295^{+36}_{-15} \mu\text{K}$.

(iv) In our pointed follow-up observation the cluster system is detected with a high significance, with each map indicating that there is a $0.6 \text{ mJy beam}^{-1}$ peak decrement ($8\sigma_{\text{SA,pointed}}$) towards the deeper component and an integrated decrement flux density ($S_{\text{SZ,integrated}}$) of $\approx 1.2 \text{ mJy beam}^{-1}$. The other component has a $0.5 \text{ mJy beam}^{-1}$ decrement and an integrated decrement of 0.7 mJy .

(v) Using the approximation $M_T^{5/3} \propto S_{\text{SZ,integrated}}$ we anticipate that the AMI blind cluster survey will detect clusters with $M_{T,200} > 2 \times 10^{14} h_{70}^{-1} M_{\odot}$ at $4\sigma_{\text{SA,survey}}$.

ACKNOWLEDGMENTS

We thank the anonymous referee for providing us with very constructive comments and suggestions. We thank PPARC/STFC for support of AMI and its operations. We are grateful to the staff of the Cavendish Laboratory and the Mullard Radio Astronomy Observatory for the maintenance and operation of AMI. CR-G, MLD, MO, MPS, TMOF and TWS acknowledge PPARC/STFC studentships. This work was performed using the Darwin Supercomputer of the University of Cambridge High Performance Computing Service (<http://www.hpc.cam.ac.uk/>), provided by Dell Inc. using Strategic Research Infrastructure Funding from the Higher Education Funding Council for England, and the Altix 3700 supercomputer at DAMTP, University of Cambridge supported by HEFCE and STFC. We are grateful to Stuart Rankin and Andrey Kaliazin for their computing assistance.

REFERENCES

AMI Consortium: Barker R. W. et al., 2006, MNRAS, 369, L1
 AMI Consortium: Davies M. L. D. et al., 2009, MNRAS, 400, 984
 AMI Consortium: Davies M. L. D. et al., 2011, MNRAS, 415, 2708
 AMI Consortium: Franzen T. M. O. et al., 2009, MNRAS, 400, 995
 AMI Consortium: Franzen T. M. O. et al., 2011, MNRAS, 415, 2699
 AMI Consortium: Hurley-Walker N. et al., 2009, MNRAS, 396, 365
 AMI Consortium: Olamaie M. et al., 2012, MNRAS, 421, 1136
 AMI Consortium: Rodríguez-González C. et al., 2011, MNRAS, 414, 3751

AMI Consortium: Scaife A. M. M. et al., 2008, MNRAS, 385, 809
 AMI Consortium: Scaife A. M. M. et al., 2009, MNRAS, 400, 1394
 AMI Consortium: Zwart J. T. L. et al., 2008, MNRAS, 391, 1545
 AMI Consortium: Zwart J. T. L. et al., 2011, MNRAS, 418, 2754
 Bartlett J. G., Silk J., 1994, ApJ, 423, 12
 Birkinshaw M., 1999, Phys. Rep., 310, 97
 Birkinshaw M., Gull S. F., Moffet A. T., 1981, ApJ, 251, 69
 Carlstrom J. E., Joy M., Grego L., 1996, ApJ, 456, L75
 Carlstrom J. E., Holder G. P., Reese E. D., 2002, ARA&A, 40, 643
 Cavaliere A., Fusco-Femiano R., 1976, A&A, 49, 137
 Cavaliere A., Fusco-Femiano R., 1978, A&A, 70, 677
 Evrard A. E. et al., 2002, ApJ, 573, 7
 Feroz F., Hobson M. P., 2008, MNRAS, 384, 499
 Feroz F., Hobson M. P., Bridges M., 2008, MNRAS, 398, 1601
 Feroz F. et al., 2009, MNRAS, 398, 2049
 Gordon C., Trotta R., 2007, MNRAS, 382, 1859
 Grainge K., Jones M., Pooley G., Saunders R., Baker J., Haynes T., Edge A., 1996, MNRAS, 333, 318
 Halverson N. W. et al., 2008, ApJ, 701, 42
 High F. W. et al., 2010, ApJ, 723, 1736
 Hincks A. D. et al., 2010, ApJS, 191, 423
 Hobson M. P., Baldwin J. E., 2004, Applied Opt., 43, 2651
 Hobson M. P., Maisinger K., 2002, MNRAS, 334, 569
 Holler C. M., Kaneko T., Jones M. E., Grainge K., Scott P., 2007, A&A, 464, 795
 Holzzapfel W. L. et al., 1997, ApJ, 479, 17
 Jeffreys H., 1961, Theory of Probability, 3rd edn. Clarendon Press, Oxford, p. 69
 Jenkins A. et al., 2001, MNRAS, 321, 372
 Jones M. E. et al., 1993, Nat, 365, 320
 Kneissl R. et al., 2001, MNRAS, 328, 783
 Komatsu E. et al., 2010, preprint (arXiv:1001.4538)
 Kosowsky A. et al., 2003, New Astron. Rev., 47, 939
 Lahav O. et al., 2002, MNRAS, 333, 961
 Lancaster K. et al., 2005, MNRAS, 359, 16
 Lancaster K. et al., 2007, MNRAS, 378, 673
 Marshall P. J., Hobson M. P., Slosar A., 2003, MNRAS, 346, 489
 Menanteau F. et al., 2010, ApJ, 723, 1523
 Muchovej S. et al., 2011, ApJ, 732, 28
 Pearson T. J. et al., 2009, BAAS, 41, 447
 Press W. H., Schechter P., 1974, ApJ, 187, 425
 Ruhl J. et al., 2004, Proc. SPIE, 5498, 11
 Seljak U. et al., 2005, Phys. Rev. D, 71, 103515
 Staniszewski Z. et al., 2009, ApJ, 701, 32
 Sunyaev R. A., Zel'dovich Ya B., 1972, Comments Astrophys. Space Phys., 4, 173
 Udomprasert P. S., Mason B. S., Readhead A. C. S., Pearson T. J., 2004, ApJ, 615, 63
 Vanderlinde K. et al., 2010, ApJ, 722, 1180
 Vikhlinin A. et al., 2009, ApJ, 692, 1060
 Waldram E. M., Pooley G. G., Davies M. L., Grainge K. J. B., Scott P. F., 2010, MNRAS, 404, 1005
 Wu J.-H. P. et al., 2009, ApJ, 694, 1619

This paper has been typeset from a $\text{\TeX}/\text{\LaTeX}$ file prepared by the author.